Numerical strategy to perform direct numerical simulations of hypersonic shock/boundary-layer interaction in chemical nonequilibrium

Pedro Stefanin Volpiani

Noname manuscript No.
(will be inserted by the editor)

Numerical strategy to perform direct numerical simulations of hypersonic shock/boundary-layer interaction in chemical nonequilibrium

Pedro Stefanin Volpiani

Received: date / Accepted: date

Abstract Literature regarding hypersonic shock/boundary-layer interaction (SBLI) is mostly restricted to calorically perfect gases, even though this condition is far from reality when temperature rises. High-temperature effects alter physical and transport properties of the fluid, due to vibrational excitation and gas dissociation, and chemical reactions must be considered in order to compute the flow field. In this work, a code for hypersonic aerodynamics with reactions using parallel machines (*CHARLIE*) is described and a numerical methodology is developed to perform direct numerical simulations of shock/boundary-layer interaction in chemical nonequilibrium. The numerical scheme and the characterization of non-reflecting boundary conditions are addressed. Results show that the flow properties differ considerably if chemical reactions are taken into account. A direct numerical simulation of a shock interacting with a turbulent boundary-layer in the hypersonic regime with high-temperature effects is also presented for the first time.

Keywords numerical methodology · hypersonic flow · shock/boundary-layer interactions · chemical nonequilibrium

1 Introduction

Understanding shock/boundary layer interactions (SBLI) is an imperative step to correctly predict the performance of hypersonic vehicles. These complex phenomena can affect considerably the aerodynamic drag and in a more drastic scenario, be responsible for low-frequency unsteadiness, leading to structural failure, loss of the control surfaces or the unstart in an engine intake. SBLI also increases the wall heat flux, a key factor when designing thermal protection systems. To ensure the safety of the space shuttle these systems are most of the time specified with a large safety factor, with the drawback of carrying extra weight. Therefore, the accurate prediction of aerodynamic heating in hypersonic flight is an important step in the design process, which can reduce the weight of the vehicle, increase the payload and enhance fuel efficiency, amongst various advantages.

The majority of the work dealing with shock/boundary-layer interaction considers a calorically perfect gas [1, 2, 3, 4, 5, 6, 7, 8, 9, 10, 11, 12, 13, 14, 15, 16, 17]. This is a reasonable hypothesis for most of experimental works employing low-enthalpy hypersonic wind tunnels. Among the experimental database of SBLI examined by Settles and Dodson [18], in terms of total enthalpy, none of the experiments matched true flight conditions. From the numerical side, a calorically perfect gas assumption makes the code much simpler, faster and more robust.

However, in hypersonic flight conditions, high-temperature effects must be taken into account in order to compute the flow field. At a pressure of 1 atm, for example, significant vibrational excitation begins at about 800 K. When temperature exceeds about 2500 K, oxygen molecules begin to dissociate while nitrogen dissociation begins at about 4000 K with significant ionization occuring at about 9000 K [19]. Despite the large number of studies dealing with high-temperature effects in hypersonic flows (see [20, 21]), the database of direct numerical simulations remains extremely limited [22, 23]. Moreover, as stated by Candler [21], little effort has been directed toward understanding turbulent motion at the extreme conditions of hypersonic flight.

Pedro Stefanin Volpiani
Department of Mechanical Engineering, University of Maryland, College Park, Maryland 20742, USA
E-mail: pedro.stefanin_volpiani@onera.fr *Present address:* ONERA, The French Aerospace Lab. 8 Rue des Vertugadins, 92190 Meudon, France

Duan and Martin [22] used direct numerical simulations (DNS) of hypersonic turbulent boundary layers to study high-enthalpy effects. More recently, Renzo and Urzay [23] studied the spatial evolution of a high-enthalpy hypersonic boundary layer from laminar to fully turbulent states. Brown [24] selected experiments of hypersonic shock/turbulent boundary layer interactions to be used as the basis for a computational sensitivity analysis. The author performed several numerical simulations, even at high-enthalpy condition, but in the framework of Reynolds Averaged Navier-Stokes (RANS) methods. Direct numerical simulations of SBLI in chemical nonequilibrium are extremely scarce for two reasons: (i) solving the steep problem introduced by the complex physics (discontinuities and reaction rates) together with the whole range of spatial and temporal scales of turbulence is not an easy task; and (ii) second, a massive amount of computational power is needed to run a single simulation. To the author's knowledge, this is the first work that discusses high-temperature effects in oblique shock/boundary-layer interactions by means of direct numerical simulations. Across the shock wave, the fluid temperature increases and is amplified for high Mach numbers and shock strengths. Therefore, such effects are likely to happen and a robust numerical method to deal with these cases is mandatory.

The immediate objective of the present work is to develop a numerical framework to perform direct numerical simulations of shock/boundary-layer interaction in chemical nonequilibrium. *CHARLIE* is a new solver that stands for Code for Hypersonic Aerodynamics with Reactions using paralleL machInEs and is carefully described in the following.

2 Conservation equations

The set of conservation equations describing the evolution of a multicomponent reactive flow is expressed in Cartesian form as

$$\partial_t \mathbf{Q} + \partial_i \mathbf{F}_i - \partial_i \mathbf{D}_i = \mathbf{\Omega} \tag{1}$$

where $\mathbf{Q} = (\rho, \rho u_1, \rho u_2, \rho u_3, \rho e, \rho Y_k)^T$ is the state vector, $\mathbf{F}_i$ the inviscid flux tensor, $\mathbf{D}_i$ the viscous flux tensor and $\mathbf{\Omega}$ the source term vector. Symbol ρ denotes the fluid density, u_i the component i of the velocity vector, e is the total energy per unit mass and Y_k is the mass fraction of species k. Using the Kronecker operator δ_{ij}, the conservative convective, diffusive and reactive vectors are defined respectively as:

$$\mathbf{F}_i = \begin{pmatrix} \rho u_i \\ \rho u_1 u_i + p\delta_{1i} \\ \rho u_2 u_i + p\delta_{2i} \\ \rho u_3 u_i + p\delta_{3i} \\ (\rho e + p) u_i \\ \rho u_i Y_k \end{pmatrix} \quad \mathbf{D}_i = \begin{pmatrix} 0 \\ \tau_{1i} \\ \tau_{2i} \\ \tau_{3i} \\ u_j \tau_{ij} - q_i \\ -J_{i,k} \end{pmatrix} \quad \mathbf{\Omega} = \begin{pmatrix} 0 \\ 0 \\ 0 \\ 0 \\ 0 \\ \dot{\omega}_k \end{pmatrix} \tag{2}$$

Since the conservation equations for all N species are computed, the mass balance equation does not need to be solved and density is given by

$$\rho = \sum_{k=1}^{N} \rho Y_k \tag{3}$$

The hydrostatic pressure p is given by the equation of state for a perfect gas:

$$p = \rho r T \tag{4}$$

where T stands for the temperature and r is the perfect gas constant per unit of mass defined as:

$$r = \frac{R}{\overline{W}}, \quad \overline{W} = \left[\sum_{k}^{N} \frac{Y_k}{W_k} \right]^{-1} \tag{5}$$

with $R = 8.314$ J/(mole K) being the gas constant, $\overline{W}$ the mean molar mass of the mixture and W_k the molar mass of species k. The stress tensor for a Newtonian fluid is given by:

$$\tau_{ij} = -\frac{2}{3}\mu \frac{\partial u_k}{\partial x_k} \delta_{ij} + \mu \left(\frac{\partial u_i}{\partial x_j} + \frac{\partial u_j}{\partial x_i} \right) \tag{6}$$

where μ is the shear viscosity. The diffusive flux of species $J_{i,k}$ is given by Fick's law:

$$J_{i,k} = -\rho D \frac{\partial Y_k}{\partial x_i} \tag{7}$$

Note that a correction velocity is usually required in Eq. (7) to respect mass conservation. However, since the diffusion coefficient D is assumed to be the same for all species, the correction velocity turns out to be zero in this particular case. This assumption may lead to inaccuracies in the diffusivity of monoatomic species like the atomic Oxygen and the atomic Nitrogen, but it is generally considered to be a good first approximation. The same approximation has been used in [22]. For multi-species flows, an additional heat flux term appears due to heat transport by species diffusion. The total heat flux vector then writes:

$$q_i = \underbrace{-\lambda \frac{\partial T}{\partial x_i}}_{\text{conduction}} + \underbrace{\sum_{k=1}^{N} J_{i,k} h_k}_{\text{species diffusion}} \tag{8}$$

where λ is the heat conduction coefficient of the mixture and h_k is the specific enthalpy of species k per unit of mass.

The thermodynamic properties of high-temperature species, including the molar heat capacity at constant pressure, enthalpy and entropy are computed with polynomial curve-fits using temperature for each species k [25]:

$$\frac{C_{p,k}}{R} = a_{1,k} + a_{2,k}T + a_{3,k}T^2 + a_{4,k}T^3 + a_{5,k}T^4 \tag{9}$$

$$\frac{H_k}{RT} = a_{1,k} + \frac{a_{2,k}}{2}T + \frac{a_{3,k}}{3}T^2 + \frac{a_{4,k}}{4}T^3 + \frac{a_{5,k}}{5}T^4 + \frac{a_{6,k}}{T} \tag{10}$$

$$\frac{S_k}{R} = a_{1,k}\ln(T) + a_{2,k}T + \frac{a_{3,k}}{2}T^2 + \frac{a_{4,k}}{3}T^3 + \frac{a_{5,k}}{4}T^4 + a_{7,k} \tag{11}$$

To recover the mass mixture properties, the species molar properties are weighted as:

$$c_p = \sum_{k=1}^{N} \frac{Y_k}{W_k} C_{p,k}\ , \quad h = \sum_{k=1}^{N} \frac{Y_k}{W_k} H_k\ , \quad s = \sum_{k=1}^{N} \frac{Y_k}{W_k} S_k \tag{12}$$

Thus, the total energy is the sum of kinetic and internal energy and is computed as:

$$e = \frac{1}{2}u_i u_i + e_{int} = \frac{1}{2}u_i u_i + \sum_{k=1}^{N}(H_k - RT)\frac{Y_k}{W_k} \tag{13}$$

The ratio of the heat capacities γ is defined as:

$$\gamma = \frac{c_p}{c_v}\ , \quad \text{with} \quad c_v = c_p - r \tag{14}$$

Pressure p is obtained from the equation of state Eq. (4) knowing T, ρ and the composition. Temperature is deduced from the internal energy e_{int} using the following first order approximation:

$$T^{n+1} = T^n + \frac{e_{int}^{n+1} - e_{int}^n}{c_v(T^n)} \tag{15}$$

where the superscript denotes the solution at iteration n and $n+1$.

In most CFD codes, the molecular viscosity μ is often assumed to be independent of the gas composition and close to that of air so that the classical Sutherland law can be used:

$$\mu = \mu_{\text{ref}} \left(\frac{T}{T_{\text{ref}}}\right)^{3/2} \frac{T_{\text{ref}} + S}{T + S} \tag{16}$$

with $\mu_{\text{ref}} = 1.716 \times 10^{-5}$ kg/(m s), $T_{\text{ref}} = 273.15$ K and $S = 110.4$ K for air. The other option is to use a power law formulation.

The thermal conductivity λ is obtained from the viscosity coefficient μ according to $\lambda = \mu c_p/\mathrm{Pr}$, with the Prandtl number taken as $\mathrm{Pr} = 0.7$. The diffusion coefficient is given by $D = \lambda/(\rho c_p \mathrm{Le})$, with unity Lewis number $\mathrm{Le} = 1$. For cases at elevated temperatures, the species viscosity μ_i and thermal conductivity λ_i are obtained from a curve fit relation:

$$\mu_i = \frac{1}{10}[\exp(C_{\mu_i})]\, T^{\left[A_{\mu_i}(\ln T)+B_{\mu_i}\right]} \tag{17}$$

$$\lambda_i = 418.4[\exp(E_{\lambda_i})]\, T^{\left[A_{\lambda_i}(\ln T)^3+B_{\lambda_i}(\ln T)^2+C_{\lambda_i}(\ln T)+D_{\lambda_i}\right]} \tag{18}$$

The curve-fit coefficients can be found in Gupta et al. [26]. To compute the viscosity and thermal conductivity of the gaseous mixture, Wilke [27]'s semi-empirical relations are used:

$$\mu = \sum_{i=1}^{N} \frac{X_i \mu_i}{\sum_{j=1}^{N} X_j \phi_{ij}} \quad , \quad \lambda = \sum_{i=1}^{N} \frac{X_i \lambda_i}{\sum_{j=1}^{N} X_j \phi_{ij}} \tag{19}$$

where X_i corresponds to the molar fraction of species i and

$$\phi_{ij} = \left[1 + \sqrt{\frac{\mu_i}{\mu_j}} \left(\frac{W_j}{W_i}\right)^{1/4}\right]^2 \left[\sqrt{8}\sqrt{1 + \frac{W_i}{W_j}}\right]^{-1}.$$

To define the chemical reaction rate expressions, we consider N species, $\mathcal{M}_k$ reacting through M reactions as:

$$\sum_{k=1}^{N} \nu_{ki}^{'} \mathcal{M}_k \rightleftharpoons \sum_{k=1}^{N} \nu_{ki}^{''} \mathcal{M}_k, \qquad i = 1, ..., M \tag{20}$$

$\nu_{ki}^{'}$ and $\nu_{ki}^{''}$ are the molar stoichiometric coefficients of species k for reaction i. The total reaction rate of species k, $\dot{\omega}_k$ is the sum of rates $\dot{\omega}_{ki}$ produced by all M reactions:

$$\dot{\omega}_k = \sum_{i=1}^{M} \dot{\omega}_{ki} = W_k \sum_{i=1}^{M} \nu_{ki} \mathcal{Q}_i \tag{21}$$

where $\nu_{ki} = \nu_{ki}^{''} - \nu_{ki}^{'}$ and $\mathcal{Q}_i$ is the rate progress of reaction i and is written:

$$\mathcal{Q}_i = K_{fi} \prod_{k=1}^{N} \left(\frac{\rho Y_k}{W_k}\right)^{\nu_{ki}^{'}} - K_{ri} \prod_{k=1}^{N} \left(\frac{\rho Y_k}{W_k}\right)^{\nu_{ki}^{''}} \tag{22}$$

K_{fi} and K_{ri} are the forward and reverse rate constants of reaction i. The forward rate constants are commonly modeled using the empirical Arrhenius law:

$$K_{fi} = A_i T^{\beta_i} \exp\left(-\frac{E_{ai}}{R_a T}\right) \tag{23}$$

Information about the pre-exponential constant A_i, the temperature exponent β_i and the activation energy E_{ai} of reaction i must be provided. R_a stands for the universal gas constant, in same units as activation energy. The reverse rate constants K_{ri} can be expressed in the same way as Eq. (23) or be computed from the forward and the equilibrium constants K_{ei} [28].

3 Numerical details

The high accuracy of the numerical methods and boundary treatments are crucial when dealing with direct and/or large eddy simulations. The numerical dispersion and dissipation errors must be minimized for all resolved wave numbers. In the present work, the system is discretized by a central finite difference scheme on a cartesian grid. It is well-known that high-order methods are unfortunately subjected to spurious numerical instabilities. These spurious short waves can be eliminated by introducing artificial dissipation through additional damping terms in the equations [29] or through employing the selective filtering technique [30, 31, 32], which does not affect the physical long waves. The latter methodology is employed for three main reasons: *i)*: it is a simple way to stabilise the numerical scheme, *ii)* the same

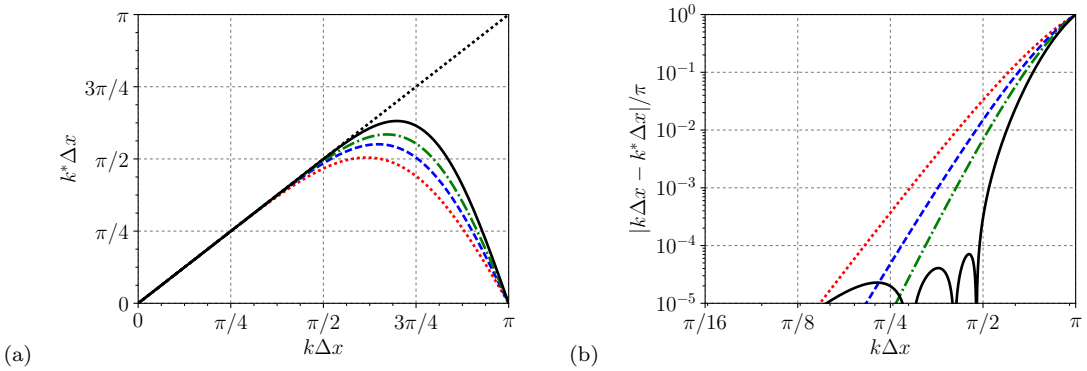

Fig. 1 Fourier analysis of central finite-difference schemes in (a) linear and (b) logarithmic scales. Optimized 4^{th} order DRP (solid), standard 10^{th} order (dashed-dotted), standard 8^{th} order (dashed) and standard 6^{th} order (dotted) schemes.

routine can be used to deal with discontinuities [33], and *iii)* in the LES context, the selective filtering alone provides an implicit model that takes into account the dissipative effect of small scales, saving computational time since no additional sub-grid scale model for the turbulent stress tensor is required [34].

3.1 Space and Time Discretizations

The spatial derivative $\partial u/\partial x$ at x_0 are approximated by a central, $2N+1$ point stencil, finite-difference scheme as

$$\frac{\partial}{\partial x}(x_0) = \frac{1}{\Delta x}\sum_{j=-N}^{N} a_j u(x_0 + j\Delta x) \tag{24}$$

where Δx is the spacing of a uniform mesh, and the coefficients a_j are such as $a_j = -a_{-j}$, providing a scheme without dissipation. The convective fluxes are discretised using a fourth-order 11-point stencil scheme optimised by Bogey and Bailly [32] and the stencil size is reduced close to the boundaries. For the viscous and heat fluxes standard fourth-order finite differences are used. Coefficients a_j can be found in Appendix 1. The effective wave number $k^*\Delta x$ of the 7-point (standard 6^{th} order), 9-point (standard 8^{th} order) and 11-point (standard 10^{th} order and optimized 4^{th} order) finite-difference schemes is plotted as a function of the reduced wave number $k\Delta x$ in Fig. 1. We note that the limit of resolvability of the optimized scheme is superior than the standard ones and is close to $k\Delta x \approx \pi/2$. The dispersion error $|k\Delta x - k^*\Delta x|/\pi$ is also very low up to $k\Delta x = \pi/2$ corresponding to 4 points per wavelength. This type of schemes is referred as dispersion relation preserving (DRP) schemes.

For a stretched grid, the spacial derivative $\partial u/\partial x$ is evaluated as

$$\frac{\partial u}{\partial x} = \frac{\partial \xi}{\partial x}\frac{\partial u}{\partial \xi} = \frac{1}{\partial x/\partial \xi}\frac{\partial u}{\partial \xi} \tag{25}$$

where ξ is an arbitrary uniform grid. At point x_0, we have

$$\frac{\partial u}{\partial x}(x_0) = \frac{1}{\widetilde{\Delta x}}\sum_{j=-N}^{N} a_j u_{0+j} \quad , \quad \text{with} \quad \widetilde{\Delta x} = \sum_{j=-N}^{N} a_j x_{0+j} \tag{26}$$

As part of the algorithm, a selective filtering is incorporated in each direction to eliminate grid-to-grid oscillations. We use an optimised filter built on an 11-point stencil from [32]. As in the previous case, the stencil size is reduced close to the boundaries. A quantity u is filtered in the $x-$direction as:

$$u^f(x_0) = u(x_0) - \chi\, D(x_0), \text{ with } D(x_0) = \sum_{j=-N}^{N} d_j u(x_0 + j\Delta x) \tag{27}$$

where the coefficients d_j are such as $d_j = d_{-j}$, ensuring no dispersion, and χ is a constant between 0 and 1. Coefficients d_j are reported in Appendix 1. Here, we keep $\chi = 0.2$ fixed. The filter damping function

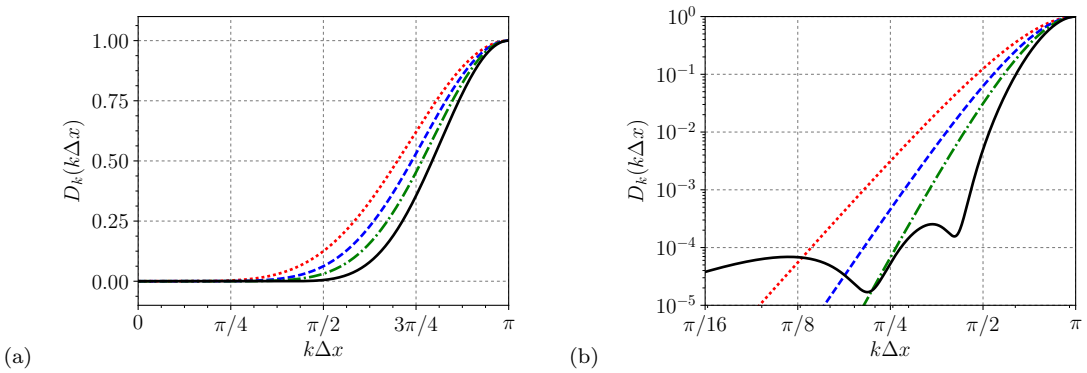

Fig. 2 Fourier analysis of filter schemes in (a) linear and (b) logarithmic scales. Optimized 11-point (solid), standard 11-point (dashed-dotted), standard 9-point (dashed) and standard 7-point stencil (dotted) schemes.

$D_k(k\Delta x)$, obtained by applying the spacial Fourier transform of D, is shown in Fig. 2 for the 7-point (standard 6^{th} order), 9-point (standard 8^{th} order), 11-point (standard 10^{th} order) and optimized 11-point stencil filters. The filter scheme has a slightly lower limit of accuracy than the finite-difference scheme. The larger scales that are accurately discretized are affected in a negligible manner by the filtering, whereas the smaller scales, poorly computed, are damped out.

The convective terms are integrated in time using an explicit low-storage six-substep Runge-Kutta scheme optimised in the wavenumber space [32]. Because of their slower time evolution, the viscous and reaction terms are only integrated in the last substep.

To improve nonlinear stability, there is an option to use the central differencing scheme in split (or "skew-symmetric") form as suggested by Ducros et al. [35]. For the species mass flux, this decomposition reads:

$$\frac{\partial \rho Y_k u_j}{\partial x_j} = \frac{1}{2}\left(\frac{\partial \rho Y_k u_j}{\partial x_j} + \rho Y_k \frac{\partial u_j}{\partial x_j} + u_j \frac{\partial \rho Y_k}{\partial x_j}\right) \tag{28}$$

3.2 Boundary conditions

Boundary conditions play a crucial role in a compressible CFD solver where acoustics is present. As a matter of fact, the time evolution of the system is governed not only by the state in the interior of the domain, but also by waves interacting with its boundary. Several studies have been carried out in the framework of non-reflecting boundary conditions to ignore non-physical waves [36, 37, 38, 39, 40, 41]. In the present solver, both inlet and outlet are treated using Navier-Stokes characteristic boundary conditions (NSCBC). Four steps are necessary to describe the NSCBC method. Firstly, the system of equations based on conservative variables must be written in the primitive form in an orthonormal base associated to the border. Then, the system can be set into characteristic form neglecting tangential, viscous and source terms. The LODI (Local One-Dimensional Inviscid) relations are used to predict the waves entering the domain that cannot be estimated by the internal points of the mesh. Finally, a change of variable is performed to the initial conservative variables and the time advancement is done taking into account all previous neglected terms.

For the sake of brevity and clarity, we will present only the analysis pertinent to a fixed boundary in the direction x_1. Terms in the x_1 direction can be recast in characteristic form to obtain:

$$\frac{\partial \rho}{\partial t} + d_1 + \frac{\partial}{\partial x_2}(\rho u_2) + \frac{\partial}{\partial x_3}(\rho u_3) = 0 \tag{29}$$

$$\frac{\partial \rho u_1}{\partial t} + u_1 d_1 + \rho d_3 + \frac{\partial}{\partial x_2}(\rho u_2 u_1) + \frac{\partial}{\partial x_3}(\rho u_3 u_1) = \frac{\partial \tau_{1j}}{\partial x_j} \tag{30}$$

$$\frac{\partial \rho u_2}{\partial t} + u_2 d_1 + \rho d_4 + \frac{\partial}{\partial x_2}(\rho u_2 u_2) + \frac{\partial}{\partial x_3}(\rho u_3 u_2) + \frac{\partial p}{\partial x_2} = \frac{\partial \tau_{2j}}{\partial x_j} \tag{31}$$

$$\frac{\partial \rho u_3}{\partial t} + u_3 d_1 + \rho d_5 + \frac{\partial}{\partial x_2}(\rho u_2 u_3) + \frac{\partial}{\partial x_3}(\rho u_3 u_3) + \frac{\partial p}{\partial x_3} = \frac{\partial \tau_{3j}}{\partial x_j} \tag{32}$$

$$\begin{aligned} &\frac{\partial \rho e}{\partial t} + \left(\frac{1}{2}u_i u_i + e_{int} + \frac{p}{\rho} - c_p T\right) d_1 + \left(\frac{c_p - r}{r}\right) d_2 + \rho u_1 d_3 + \rho u_2 d_4 + \rho u_3 d_5 + \\ &\sum_{k=1}^{N} \left(\rho h_k - p\frac{\overline{W}}{W_k}\frac{c_p}{r}\right) d_5 + \frac{\partial}{\partial x_2}[u_2(\rho e + p)] + \frac{\partial}{\partial x_3}[u_3(\rho e + p)] = \frac{\partial (u_j \tau_{ij})}{\partial x_i} - \frac{\partial q_i}{\partial x_i} \end{aligned} \tag{33}$$

$$\frac{\partial \rho Y_k}{\partial t} + Y_k d_1 + \rho d_{5+k} + \frac{\partial}{\partial x_2}(\rho u_2 Y_k) + \frac{\partial}{\partial x_3}(\rho u_3 Y_k) = \dot{\omega}_k \tag{34}$$

Note that the formulation presented by Pakdee and Mahalingam [41] is retained here, for reasons to be discussed later. The different terms of system (34) contain derivatives normal to the x_1 boundary (d_1 to d_{5+k}), derivatives parallel to the x_1 boundary, and local viscous and reaction terms.

The vector $\mathbf{d}$ is given by characteristic analysis [38]:

$$\begin{pmatrix} d_1 \\ d_2 \\ d_3 \\ d_4 \\ d_5 \\ d_{5+k} \end{pmatrix} = \begin{pmatrix} \frac{1}{c^2}\left[\mathcal{L}_2 + \frac{1}{2}(\mathcal{L}_5 + \mathcal{L}_1)\right] \\ \frac{1}{2}(\mathcal{L}_5 + \mathcal{L}_1) \\ \frac{1}{2\rho c}(\mathcal{L}_5 - \mathcal{L}_1) \\ \mathcal{L}_3 \\ \mathcal{L}_4 \\ \mathcal{L}_{5+k} \end{pmatrix} \quad \text{with} \quad \begin{pmatrix} \mathcal{L}_1 = (u_1 - c)\left(\frac{\partial p}{\partial x_1} - \rho c \frac{\partial u_1}{\partial x_1}\right) \\ \mathcal{L}_2 = u_1\left(c^2 \frac{\partial \rho}{\partial x_1} - \frac{\partial p}{\partial x_1}\right) \\ \mathcal{L}_3 = u_1 \frac{\partial u_2}{\partial x_1} \\ \mathcal{L}_4 = u_1 \frac{\partial u_3}{\partial x_1} \\ \mathcal{L}_5 = (u_1 + c)\left(\frac{\partial p}{\partial x_1} + \rho c \frac{\partial u_1}{\partial x_1}\right) \\ \mathcal{L}_{5+k} = u_1 \frac{\partial Y_k}{\partial x_1} \end{pmatrix} \tag{35}$$

where c is the local sound speed. $\mathcal{L}_1$ and $\mathcal{L}_5$ correspond respectively to left- and right-going acoustic waves. The local one dimensional inviscid (LODI) relations can be cast in terms of primitive variables as:

$$\begin{aligned} \frac{\partial \rho}{\partial t} + \frac{1}{c^2}\left[\mathcal{L}_2 + \frac{1}{2}(\mathcal{L}_5 + \mathcal{L}_1)\right] &= 0 \\ \frac{\partial p}{\partial t} + \frac{1}{2}(\mathcal{L}_5 + \mathcal{L}_1) &= 0 \\ \frac{\partial u_1}{\partial t} + \frac{1}{2\rho c}(\mathcal{L}_5 - \mathcal{L}_1) &= 0 \\ \frac{\partial u_2}{\partial t} + \mathcal{L}_3 &= 0 \\ \frac{\partial u_3}{\partial t} + \mathcal{L}_4 &= 0 \\ \frac{\partial Y_k}{\partial t} + \mathcal{L}_{5+k} &= 0 \end{aligned} \tag{36}$$

At the outlet, the characteristic boundary condition is non-reflective by imposing $\mathcal{L}_1 = 0$. At the inlet of a SBLI simulation the variables can be imposed in a "hard way", since the incoming flow is supersonic. Note that other methods exist to obtain non-reflective boundary conditions [42].

At the wall, we impose $\partial p/\partial y = 0$ and $u_i = 0$. In 3D, the conservative flux can be expressed in a simple form:

$$\mathbf{F} = \begin{Bmatrix} \rho\dfrac{\partial u_2}{\partial y} \\ \rho u_1\dfrac{\partial u_2}{\partial y} \\ 0 \\ \rho u_3\dfrac{\partial u_2}{\partial y} \\ p\dfrac{\partial u_2}{\partial y} + \dfrac{\rho(u_1^2+u_3^2)}{2}\dfrac{\partial u_2}{\partial y} + \rho e_{int}\dfrac{\partial u_2}{\partial y} \\ \rho Y_k\dfrac{\partial u_2}{\partial y} \end{Bmatrix} \tag{37}$$

The derivative $\partial u_2/\partial y$ is computed using a decentered scheme of order 2:

$$\frac{\partial u_2}{\partial y} = \frac{4u_{2,\mathrm{w}+1} - u_{2,\mathrm{w}+2}}{2\Delta y} \quad \text{with} \quad u_{2,\mathrm{w}} = 0 \tag{38}$$

For the species, we consider a non-catalytic surface by imposing $(\partial Y_k/\partial y)_{\mathrm{w}} = 0$. A sponge zone is also imposed in the outlet region combining grid stretching and a Laplacian filter in the streamwise direction following [43].

4 Validation test-cases

4.1 2D shock/boundary-layer interaction from Degrez et al. [44]

A laminar shock boundary-layer interaction, investigated both experimentally and numerically by Degrez et al. [44], was chosen to validate the solver using realistic thermodynamic properties. In their experiment, the freestream Mach number was $\mathrm{Ma}_\infty = 2.2$ and the shock generator angle $\vartheta = 3.75°$. The stagnation pressure and temperature were respectively $p_0 = 0.107$ bar and $T_0 = 293$ K. The authors observed discrepancies between their simulations and experiments, attributed to a slight incidence angle of the flat plate (less than 1°) and a non-uniformity in the test-section Mach number. To obtain a better match between measurements and simulations, the freestream Mach number was reduced to $\mathrm{Ma}_\infty = 2.15$ and the wedge angle increased to $\vartheta = 3.81°$. The same conditions were used in our simulations. Thus, the shock impacts the adiabatic flat plate at a position $x_{\mathrm{sh}} = 0.08$ m from the leading edge with an angle of 30.8°. Assuming a specific heat ratio of $\gamma = 1.4$, the freestream pressure and temperature are respectively $p_\infty = 1082$ Pa and $T_\infty = 152.24$ K, based on the stagnation values. The Reynolds number based on the distance from the plate edge to the shock impingement position is $\mathrm{Re} = 10^5$.

The computational grid contains 180×300 points with cell sizes of $\Delta x = 5\times10^{-4}$ and $\Delta y_{\min} = 5\times10^{-5}$ m. The grid stretching in the normal direction is 1.02. Flow visualisations are provided in Fig. 3, where the density and streamwise velocity distributions are shown.

The longitudinal evolution of the wall pressure and friction coefficient are compared with Degrez et al.'s results in Fig. 4. The shift in the pressure signal in Fig. 4(a) can be explained by the presence of the leading shock in the present numerical simulation, which yields a higher upstream pressure than in the experiment. The discordance between the present results and the simulation presented in the original article in Fig. 4(b) can be explained by the difference in the grid resolution. Other works also found the same discrepancy [45, 46]. In order to overcome any doubts, an additional simulation has been done using the *Hybrid* solver [47, 48]. Differently from the present code, to approximate the inviscid fluxes *Hybrid* uses a fifth-order accurate weighted essentially non-oscillatory WENO scheme with Roe flux splitting in sharp regions, and a sixth-order accurate central difference scheme on the split form by Ducros *et al.* [35] in the remainder of the domain. All computational parameters remained the same. The agreement between both runs is excellent and shows that the shock-capturing schemes do not affect the quality of the solution, nor the position or size of the recirculation bubble. Velocity profiles are compared with Degrez et al.'s computational results in Fig. 5. Despite the mismatch of the skin friction distribution, the agreement between velocity profiles is quite good.

Before moving to the next test case, the implementation of characteristic boundary condition in the present solver is discussed. Formulations proposed by Poinsot and Lele [38] and Pakdee and Mahalingam [41] were tested in this study. The latter was found to be more robust to specify boundary conditions for

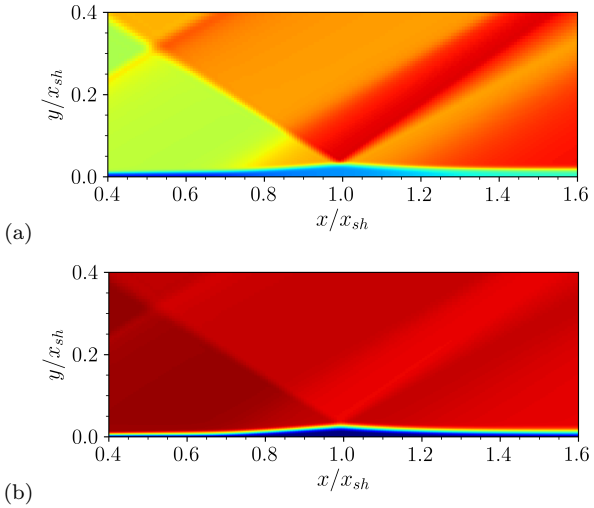

Fig. 3 Numerical simulation of the laminar shock/boundary-layer interaction studied experimentally by Degrez et al. [44]. (a) Density and (b) streamwise velocity fields.

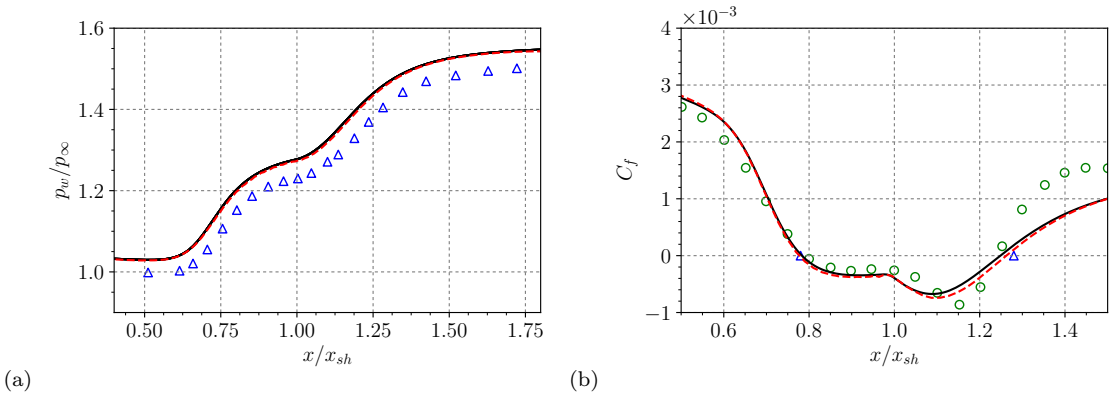

Fig. 4 Longitudinal evolution of the (a) wall pressure and (b) friction coefficient: present code (solid), *Hybrid* code (dashed), Degrez et al.'s experimental results (triangles), Degrez et al.'s computational results (circles).

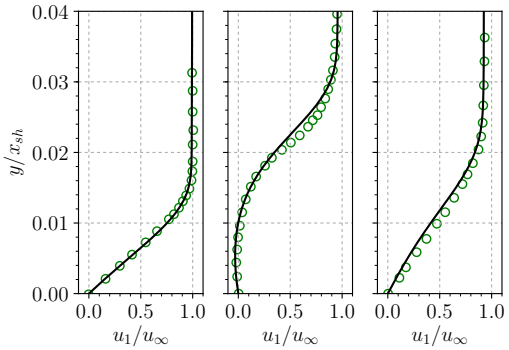

Fig. 5 Comparison of velocity profiles: present code (solid), Degrez et al.'s computational results (circles) at stations $x/x_{\mathrm{sh}} = 0.6$ (left), $x/x_{\mathrm{sh}} = 0.95$ (middle) and $x/x_{\mathrm{sh}} = 1.6$ (right).

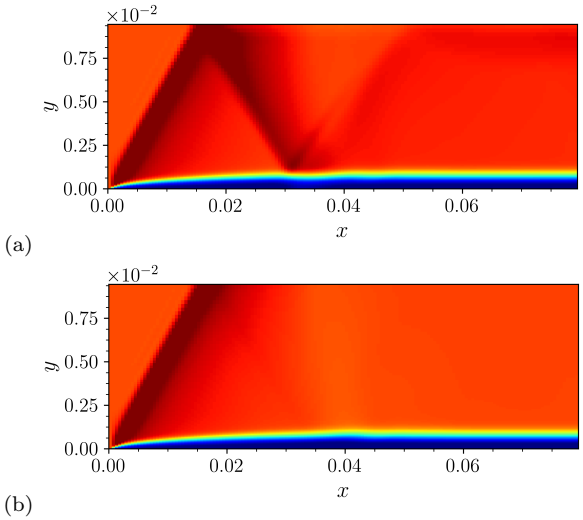

Fig. 6 Instanteneous snapshots of the density field for the laminar boundary-layer test-case. (a) Classic NSCBC [38] and (b) modified NSCBC [41].

flows with realistic thermodynamic properties. Most cases presented in the literature treats simple one-dimensional problems or two-dimensional vortex pair propagation. Here the laminar supersonic boundary layer at Mach number $\mathrm{Ma}_\infty = 2.15$ was simulated to test the outflow boundary condition, since it is closer to the flow of interest. The mesh resolution from the laminar SBLI test-case was maintained. This configuration exhibits a compression shock generated at the inflow station. For the classic NSCBC [38], the shock is reflected backwards. The new methodology correctly suppresses the shock as indicated in Fig. 6. It is worth noting that the original method has been evolving over the years and has been extensively used in industrial configurations. These cases usually do not involve shocks crossing boundaries and they use coarsened meshes closed to outlets. For a more detailed discussion on the NSCBC method, the reader is referred to other works in the area such as [49, 50].

4.2 Turbulent boundary layer

The specification of realistic inflow turbulence plays an important role, when simulating wall-bounded flows with high-fidelity methods. In this work, synthetic inflow turbulence is generated using the digital filtering technique by Klein et al. [51], Xie and Castro [52] and Touber and Sandham [11]. The synthetic digital filtering method introduces spatial/temporal coherence to randomly generate fluctuating fields through a low-pass filtering procedure that enforces approximate integral length/time scales. These fluctuations are further scaled in magnitude to recover specified Reynolds stresses and added to the specified mean boundary layer inflow profile, yielding the desired turbulent inflow boundary condition. The steps of the methodology are illustrated in Fig. 7.

We generate three independent random array sequences to seed the simulation inflow plane every time step. Each sequence is produced based on the Box-Muller transform. This step is represented in Fig. 7a. Once we have the normally distributed random numbers with zero mean and unit variance, we filter each field in the spanwise (z, Fig. 7b) and wall-normal (y, Fig. 7c) directions, respectively. Although previous studies use different filter sizes (and length scales) for the inner and outer parts of the boundary layer, Adler et al. [53] showed that these are unnecessary complications, as all the strategies result in similar development lengths, with shorter lengths required for larger Reynolds number. In their simulation, they assumed equality of the wall normal and spanwise integral lengths in the outer layer and they explained that close to the wall, the wall normal integral lengths are naturally reduced, due to the finer mesh resolution. Here, filtering length scales of $(I_x, I_y, I_z = 0.6, 0.2, 0.2)\delta_{\mathrm{in}}$ are used. Additionally, since larger (integral) scales must be supported at the inlet plane, in order to reduce the cost of filtering, we perform the procedure on a separate coarser inflow plane, in both y and z directions, followed by linear interpolation as suggested in [53]. To establish the streamwise correlation, the filtered random inlet data at iteration n is correlated to the inlet fluctuations at the previous iteration $n-1$ as in [11] (except at the beginning of the simulation). This allows us to avoid the expensive three-dimensional filtering originally suggested by Klein et al. [51]. Before introducing the correlated random fluctuations

Table 1 Global characteristics of the turbulent boundary layers at $40\delta_{\text{in}}$. The Reynolds numbers are defined as $\text{Re}_\theta = \rho_\infty u_\infty \theta/\mu_\infty$, $\text{Re}_{\delta_2} = \rho_\infty u_\infty \theta/\mu_\text{w}$, $\text{Re}_\tau = \rho_\text{w} u_\tau \delta/\mu_\text{w}$ where θ is the momentum thickness and u_τ the friction velocity.

Simulation	Ma_∞	p_∞ [Pa]	T_∞ [K]	Re_θ	Re_{δ_2}	Re_τ	δ_{in} [mm]
BL	2.28	23999	169.44	1110	650	218	0.3

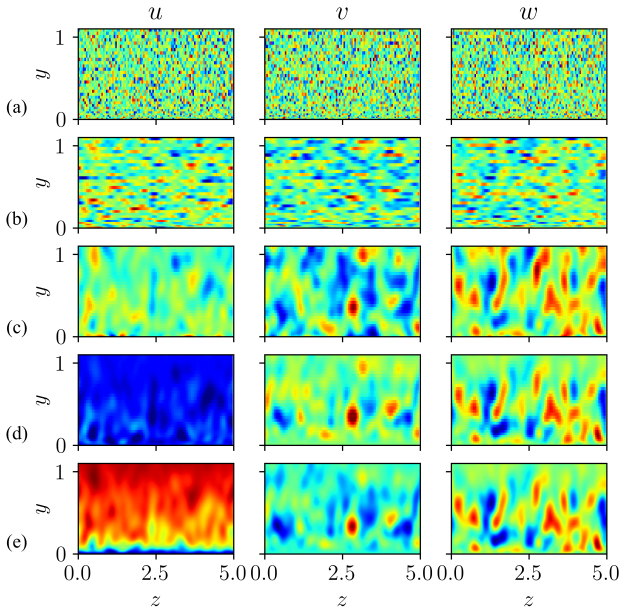

Fig. 7 Steps for the turbulence inflow generation. (a) Generate random fluctuations. (b) Filter in the spanwize and (c) wall-normal direction. (d) Apply Cholesky transformation. (e) Add the mean inlet velocity profile.

at the inlet, a transformation based on the Cholesky decomposition of the Reynolds stress tensor R_{ij} is applied following [54] (Fig. 7d). This step ensures that the velocity fluctuations at the inlet will satisfy a prescribed Reynolds stress tensor. Finally, the velocity fluctuations are added to the prescribed mean inlet velocity profile to get the instantaneous inlet velocity field (Fig. 7e).

In order to validate the inflow condition, we perform a DNS of an adiabatic supersonic boundary layer at low Reynolds number and compare the results with the incompressible database of Schlatter and Örlü [55]. A summary of physical parameters for this test-case is given in Table 1. The computational domain has an overall extent $L_x \times L_y \times L_z = 60\delta_{\text{in}} \times 9\delta_{\text{in}} \times 5\delta_{\text{in}}$, where δ_{in} is the boundary layer thickness at the inlet. Grid nodes are uniformly distributed in the spanwise (z) and streamwise (x) directions. For the wall-normal direction (y), the grid stretching is 1.015. The grid contains $800 \times 256 \times 128$ points and the grid spacing in terms of wall units in each directions is $(\Delta x^+, \Delta y_\text{w}^+, \Delta z^+) = (9.3, 0.5, 4.8)$.

Figure 8(a) shows the Van Driest transformed mean velocity profile for the simulation with an adiabatic wall at $40\delta_{\text{in}}$. The Reynolds numbers at this station are listed in Table 1. The density-scaled Reynolds stresses are shown in Fig. 8(b). The incompressible DNS results of Schlatter and Örlü [55] at a similar Reynolds number ($\text{Re}_\theta = \text{Re}_{\delta_2} = 670$ and $\text{Re}_\tau = 250$) is also shown in Fig. 8 and compare well with the present mean velocity and root-mean-square profiles.

The streamwise evolution of the skin friction coefficient is a good indicator to judge the convergence toward a fully developed turbulent boundary layer. The van Driest II transformation of the friction coefficient is compared in Fig. 9(a) with the incompressible Karman/Schoenherr and Blasius correlations [58]. The incompressible friction coefficient is obtained by

$$C_{fi} = \frac{C_f(T_\text{w}/T_\infty - 1)}{\arcsin^2 \alpha} \quad \text{with} \quad \alpha = \frac{(T_\text{w}/T_\infty - 1)}{\sqrt{T_\text{w}/T_\infty\,(T_\text{w}/T_\infty - 1)}} \tag{39}$$

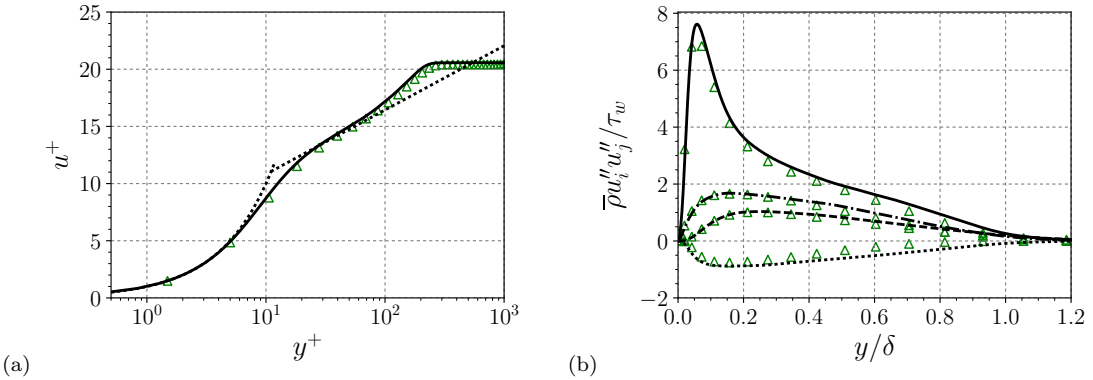

Fig. 8 (a) Van Driest transformed mean velocity profile (solid line). The linear $u^+ = y^+$ and log-law $u^+ = 5.2 + 2.44 \ln y^+$ are also represented (dotted lines). (b) Density-scaled Reynolds stress components: longitudinal (solid), wall-normal (dashed), transverse (dot-dashed) and shear stress (dotted line). Symbols: incompressible DNS results from Schlatter and Örlü [55] at a similar Reynolds number ($\mathrm{Re}_\theta = \mathrm{Re}_{\delta_2} = 670$ and $\mathrm{Re}_\tau = 250$).

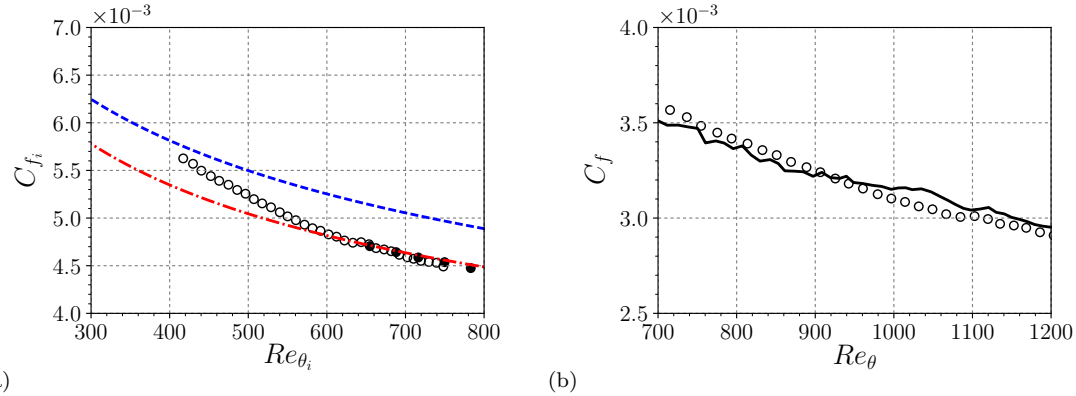

Fig. 9 Comparison of DNS data with theoretical correlations. (a) Incompressible friction coefficient and (b) compressible friction coefficient. Present DNS (empty symbols). DNS from Pirozzoli and Bernardini [56] (filled symbols). DNS from Volpiani et al. [57] (solid line). Karman/Schoenherr correlation (red dash-dotted line). Blasius correlation (blue dashed line).

The incompressible Reynolds number is given by $\mathrm{Re}_{\theta i} = \mathrm{Re}_\theta \, \mu_\infty / \mu_\mathrm{w}$. The Karman/Schoenherr Cf_{KS} and Blasius Cf_B correlations are obtained by

$$C_{fKS} = \frac{1}{17.08(\log_{10} Re_{\theta i})^2 + 25.11 \log_{10} Re_{\theta i} + 6.012} \quad \text{and} \quad C_{fB} = \frac{0.026}{Re_{\theta i}^{1/4}} \tag{40}$$

For reference purposes, we also report the DNS data of Pirozzoli and Bernardini [56] in filled symbols. The agreement is excellent between theoretical correlations and numerical results confirming the fully turbulent state of the boundary layer. We plot in Fig. 9(b) the friction coefficient as a function of Re_θ together with numerical results from Volpiani et al. [57]. Once again, we confirm that the present inflow boundary condition and the development length of $40\delta_\mathrm{in}$ are sufficient to produce realistic turbulence.

A full validation of the thermo-chemistry implementation is given in Appendix 2.

5 Simulation of a hypersonic SBLI in chemical nonequilibrium

In this section, two- and three-dimensional SBLI simulations in chemical nonequilibrium are tested. For these simulations, the option of calculating the convective fluxes using the split form was activated. As already mentioned, the literature dealing with the canonical case of a shock impinging over a boundary layer is basically restricted to the calorically perfect gas assumption and does not take into account chemical reactions. In the present simulation, the free-stream Mach number was chosen to be $\mathrm{Ma}_\infty = 5.6$ and the deflection angle $\vartheta = 6°$. The incoming laminar boundary layer is modelled, for simplicity and easily reproduction, using a fourth order polynomial approximation of the Blasius profile, defined as [59]

Table 2 Flow parameters of hypersonic SBLI.

Ma_∞	ρ_∞ [kg/m^3]	T_∞ [K]	T_w [K]	u_∞ [m/s]	ϑ [°]
5.6	0.0224	2275	3042	5150	6

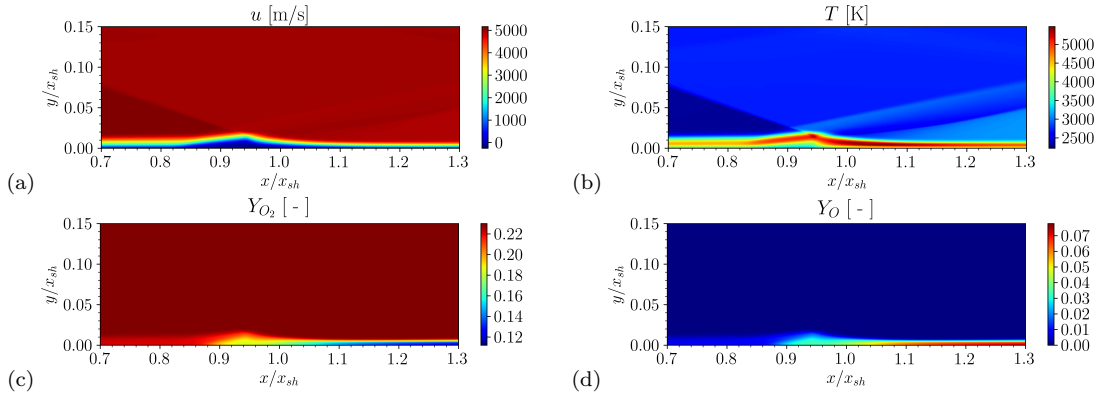

Fig. 10 Flow visualisation for the laminar SBLI in chemical nonequilibrium: (a) streamwise velocity, (b) temperature, (c) mass fraction of O_2 and (d) mass fraction of O.

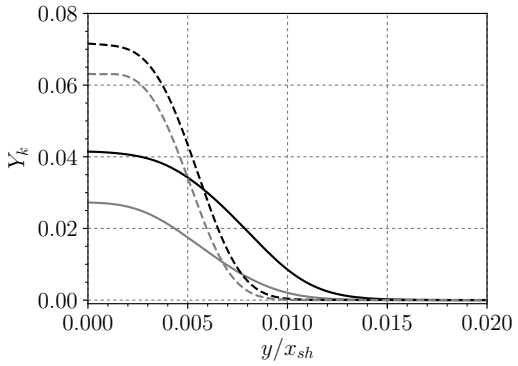

Fig. 11 Mass fraction profiles for O (black) and NO (gray) at $x/x_\mathrm{sh} = 1.$ (solid) and $x/x_\mathrm{sh} = 1.3$ (dashed lines).

$$\frac{u_1(y)}{u_\infty} = \frac{y}{\delta_\mathrm{in}}\left[2 - 2\left(\frac{y}{\delta_\mathrm{in}}\right)^2 + \left(\frac{y}{\delta_\mathrm{in}}\right)^3\right] \tag{41}$$

where y is the wall-normal direction and δ_in the boundary layer thickness, taken as $\delta_\mathrm{in} = 1$ mm. The Rankine-Hugoniot relations are used to create an oblique shock at the inlet plane. At the inlet, the species mass fractions are initialized to their equilibrium values as done in [60]. No-slip condition is applied on the lower boundary and the wall temperature is kept at $T_\mathrm{w} = 3042$ K. A non-reflecting outlet boundary condition was used together with a sponge zone. The flow parameters are given in Table 2 and they are similar to those reported in [61]. The reaction coefficients can be found in Table 3.

The computational domain is discretised using 1000×280 points with cell sizes of $\Delta x = 0.2$ and $\Delta y_\mathrm{min} = 0.01$ mm and extents over $200\delta_\mathrm{in} \times 40\delta_\mathrm{in}$. In the wall-normal direction, a 1.5% geometrical stretching is applied. A grid refinement study confirmed that the solution was grid independent.

Flow visualisations are provided in Fig. 10 for the streamwise velocity, temperature and mass fractions of O_2 and O. The temperature is high in the hypersonic boundary layer reaching temperatures of around 4500 K, but as expected, it is even higher in the shock region reaching temperatures of 5500 K. The mass fraction profiles for O and NO is given in Fig. 11 at two different locations: $x/x_\mathrm{sh} = 1.$ and $x/x_\mathrm{sh} = 1.3$. We note that downstream of the interaction, the production rate of these species increases. The wall pressure normalized by the free-stream pressure and the skin friction coefficient are plotted in Fig. 12

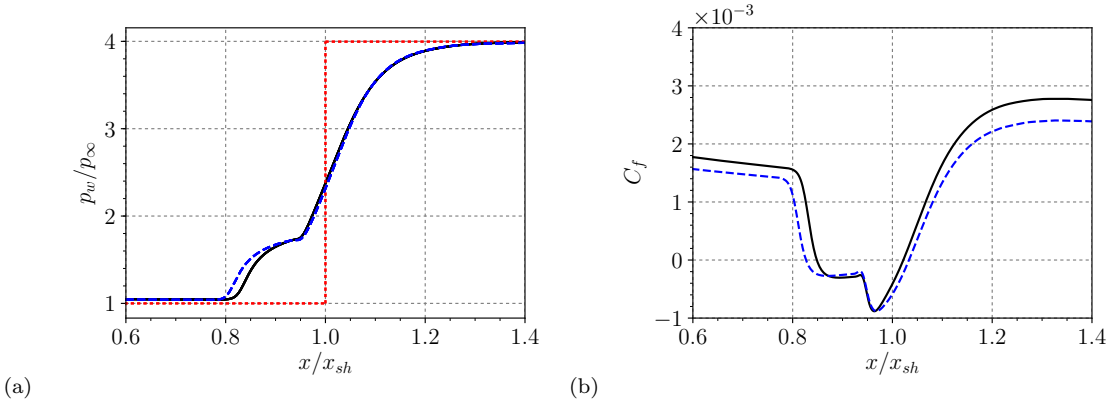

Fig. 12 Longitudinal evolution of the (a) wall pressure and (b) friction coefficient. Solid: simulation considering 5 reacting species. Dashed: case without reaction using the classic Sutherland law and variable thermodynamic properties. Dotted line indicates the inviscid pressure jump.

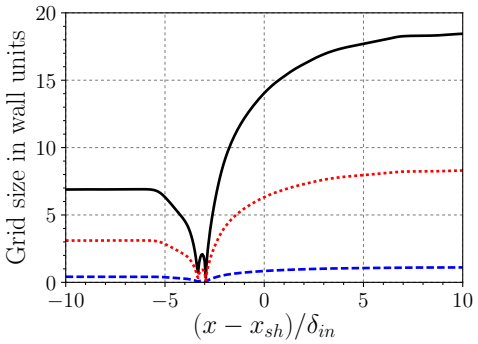

Fig. 13 Resolution in wall units along the wall. Δx^+ (solid), Δy_w^+ (dashed), Δz^+ (dotted line).

for the simulation with and without reactions. The difference between both cases is quite large and is supposed to increase for stronger interactions. A similar trend was also found in the RANS simulations of Brown [24]. The pressure jump predicted by the inviscid theory is also plotted in the figure for $\gamma = 1.29$. Despite the fact that the flow is not calorically perfect, the difference between the final values is very small. Note that the pressure starts to increase where the flow detaches. For the reactive case, the flow separates at $x/x_{\mathrm{sh}} \approx 0.85$ and reattaches at $x/x_{\mathrm{sh}} \approx 1.02$.

To prove the capability of the methodology to simulate three-dimensional SBLI in chemical nonequilibrium, the flow properties were kept unchanged but now the oblique shock impinges over a turbulent boundary layer. The computational domain has an overall extent $L_x \times L_y \times L_z = 65\delta_{\mathrm{in}} \times 9\delta_{\mathrm{in}} \times 5\delta_{\mathrm{in}}$, where $\delta_{\mathrm{in}} = 3$mm is the boundary layer thickness at the inlet. In order to keep the DNS resolution throughout the entire domain, the Reynolds number was kept low ($\mathrm{Re}_\tau = 190$). Despite the low Reynolds number, the simulation ran for 15 days on 800 Ivy Bridge 2.8 GHz processors. The grid contains $1200 \times 256 \times 200$ points and the grid spacing in terms of wall units in each direction before the interaction is $(\Delta x^+, \Delta y_{\mathrm{w}}^+, \Delta z^+) = (6.8, 0.4, 3.1)$. It is important to note that the viscous length scale decreases after the interaction [62] as shown in Fig. 13. Note that, even in the post-shock region, the grid has a similar resolution than the one presented in [22].

To provide an overview of the flow topology, a snapshot of this three-dimensional configuration is reported in Fig. 14. The incident and reflecting shocks are identified by plotting an iso-surface of dilatation. In Fig 14a, an iso-surface of the Q-criterion is coloured by the streamwise velocity u and in Fig. 14b by the mass fraction Y_O. We note that the turbulence activity is clearly modified after the reflecting shock foot and most of the reaction takes place after the interaction. These findings are also verified by analysing the mean and the root-mean-square (RMS) quantities of velocity and oxygen in Fig. 15. We emphasize the fact that the characteristics of the turbulent activity within the interaction is consistent with other numerical studies [57].

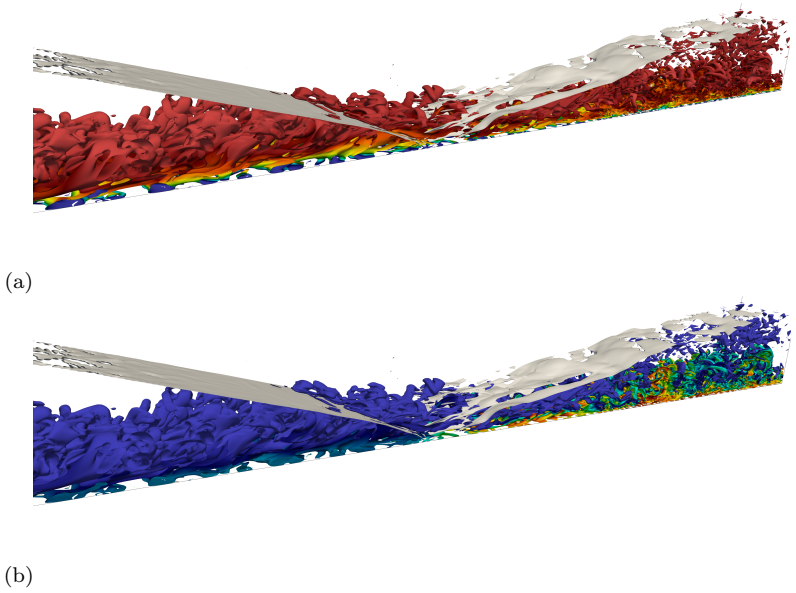

(a)

(b)

Fig. 14 Instantaneous fields of an oblique shock interacting with a turbulent boundary layer in chemical non-equilibrium. Iso-surface of the Q-criterion coloured by the (a) streamwise velocity and (b) Y_O. The dilatation iso-surface is shown in gray.

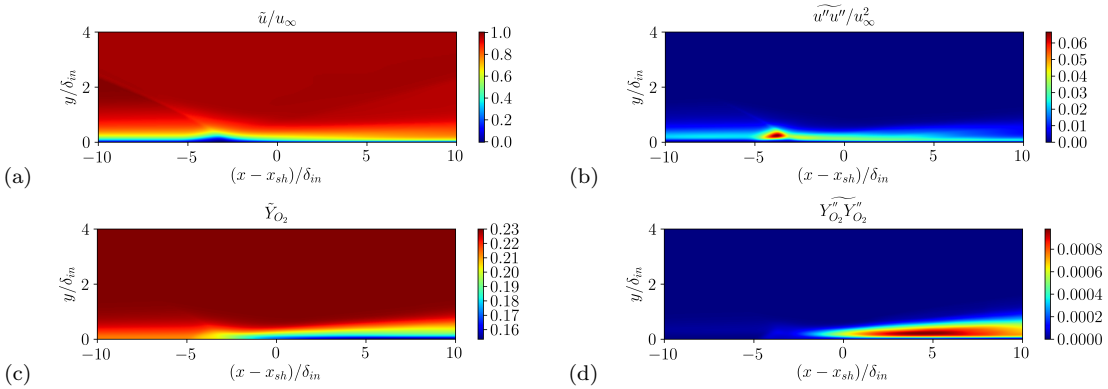

Fig. 15 Oblique shock interacting with a turbulent boundary layer in chemical non-equilibrium. (a) Mean and (b) root-mean-square fields for the streamwise velocity and (c) mean and (d) root-mean-square fields for the oxygen mass fraction Y_{O_2}.

Figure 16 displays the wall-normal profile of the mean temperature and its RMS fluctuations in the incoming boundary layer at station $x/x_{\text{sh}} = 0.7$. Note that the trend of the mean temperature is non-monotonic and this is due to the effect of aerodynamic heating in the presence of the cold wall. Moreover, the high temperature in the boundary layer, even before the interaction, is responsible for gas dissociation (see Fig. 17). The wall-normal profiles of the temperature fluctuations are characterized by two peaks and is in agreement with other studies dealing with hypersonic turbulent boundary layers at low and high enthalpies [22, 23]. The wall-normal profiles of the mean and RMS fluctuations of oxygen mass fractions before and within the interaction region are shown in Fig. 17. In the near-wall region of the undisturbed boundary layer, diatomic oxygen dissociates due to the elevated temperature. Within the interaction, reactions are stronger and the level of fluctuations are higher. Away from the wall, mass fraction fluctuations disappear. Similar conclusions can be drawn for other species, such as NO (Fig. 18).

Figure 19 shows the mean skin friction coefficient, wall pressure and Stanton number distribution for the reactive shock/boundary-layer interaction. It is worth mentioning that the Reynolds analogy factor defined as $R_{af} = 2C_h/C_f$, where C_f is the skin friction coefficient and C_h the Stanton number, is equal to 1.18 before the interaction indicating that the boundary layer is fully turbulent. This value is extremely close to the ones obtained by Duan and Martin [22] in their DNS of reactive boundary layers (1.17-1.21). Hypersonic experimental data indicates that $0.9 < R_{af} < 1.3$ [63]. Figure 19(a) indicates that, in an average sense, the flow practically remains attached. Figure 19(b) shows that the pressure signal

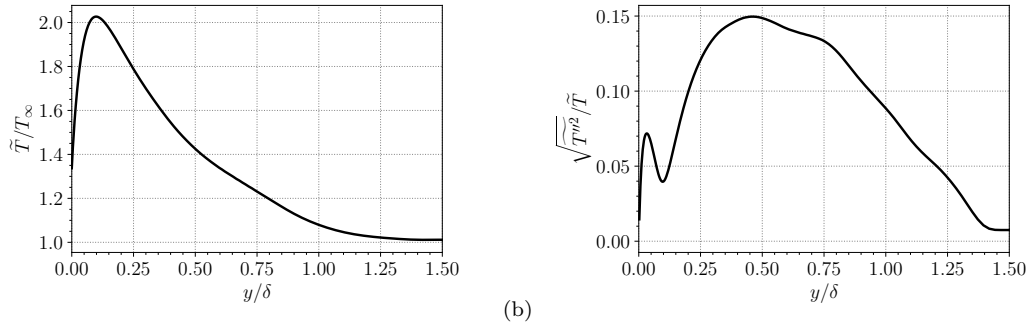

(a) (b)

Fig. 16 Wall-normal profiles of (a) Favre mean temperature and (b) RMS of Favre fluctuations of temperature at $x/x_{\mathrm{sh}} = 0.7$.

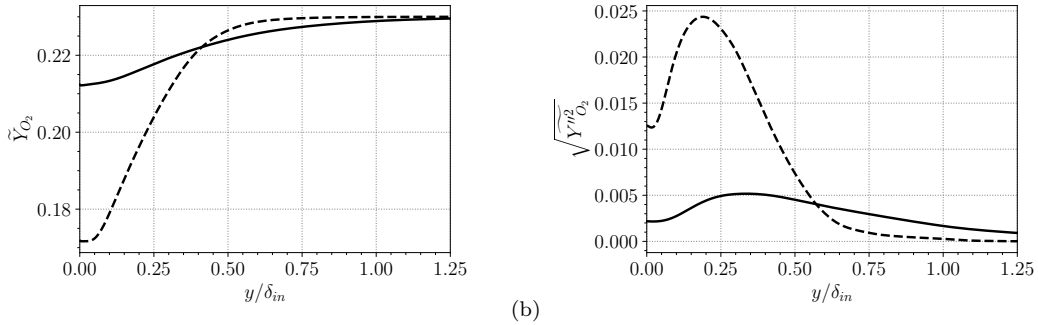

(a) (b)

Fig. 17 (a) Favre mean and (b) RMS of Favre fluctuations of O_2 mass fraction profiles at $x/x_{\mathrm{sh}} = 0.8$ (solid) and $x/x_{\mathrm{sh}} = 1.$ (dashed lines).

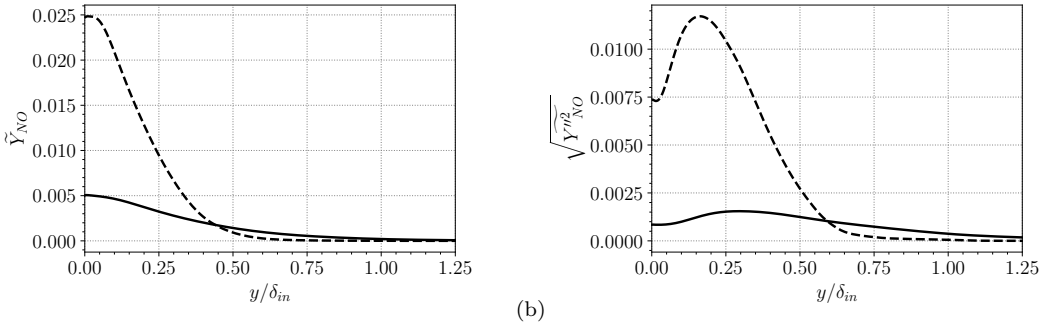

(a) (b)

Fig. 18 (a) Favre mean and (b) RMS of Favre fluctuations of NO mass fraction profiles at $x/x_{\mathrm{sh}} = 0.8$ (solid) and $x/x_{\mathrm{sh}} = 1.$ (dashed lines).

increases smoothly and does not exhibit a plateau. The same patterns were noticed in other studies dealing with weak interactions at similar Mach numbers [62, 15]. In Fig. 19(c), the Stanton number distribution C_h reaches its minimum value close to the separation point and then it sharply increases within the interaction zone. Hayashi et al. [64] observed the same behaviour in their non-reactive experiment at $\mathrm{Ma}_\infty = 4$.

In the future, high-fidelity simulations using multi/single species, different transport properties, and thermodynamics should be investigated. Since the size of the separation region is linked to the state of the incoming boundary layer [65, 66, 57, 62], if the fluid properties are modified, differences in the mean flow field are expected to happen (as shown by the two-dimensional study). Moreover, it is worth noting that the 7-coefficient polynomials, used to compute the pure species heat capacities, enthalpies, and entropies, are valid for most of the species up to 6000 K, which is in agreement with the conditions presented in the paper. However, if higher shock strengths (and consequently higher post-shock temperatures) are considered, one should deploy the 9-coefficient polynomials that extend the validity of thermodynamics properties up to 20000 K.

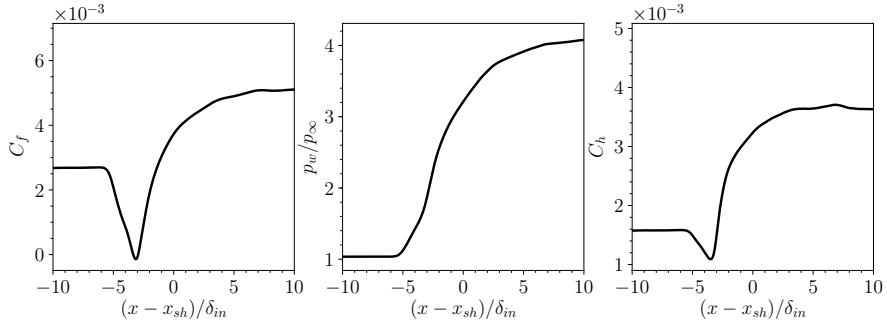

Fig. 19 Distribution of the mean skin friction coefficient (left), wall pressure (middle) and Stanton number (right) for the reactive shock/boundary-layer interaction.

Table 3 Kinetic mechanism for high-temperature air for the Dunn/Kang model [67, 19]. Activation energies are in cal/mol and pre-exponential constants in cgs units. Subscript f stands for the forward reaction and b for the backward reaction.

Reaction	A_f	β_f	E_{af}	A_b	β_b	E_{ab}
$O_2 + N \longleftrightarrow 2O + N$	3.6×10^{18}	-1.0	118800.0	3.0×10^{15}	-0.5	0.0
$O_2 + NO \longleftrightarrow 2O + NO$	3.6×10^{18}	-1.0	118800.0	3.0×10^{15}	-0.5	0.0
$O_2 + N_2 \longleftrightarrow 2O + N_2$	7.2×10^{18}	-1.0	119000.0	6.0×10^{15}	-0.5	0.0
$O_2 + O \longleftrightarrow 2O + O$	9.0×10^{19}	-1.0	119000.0	7.5×10^{16}	-0.5	0.0
$O_2 + O_2 \longleftrightarrow 2O + O_2$	3.24×10^{19}	-1.0	119000.0	2.7×10^{16}	-0.5	0.0
$N_2 + O \longleftrightarrow {}_2N + O$	1.9×10^{17}	-0.5	226000.0	1.1×10^{16}	-0.5	0.0
$N_2 + NO \longleftrightarrow 2N + NO$	1.9×10^{17}	-0.5	226000.0	1.1×10^{16}	-0.5	0.0
$N_2 + O_2 \longleftrightarrow 2N + O_2$	1.9×10^{17}	-0.5	226000.0	1.1×10^{16}	-0.5	0.0
$N_2 + N \longleftrightarrow 2N + N$	4.085×10^{22}	-1.5	226000.0	2.27×10^{21}	-1.5	0.0
$N_2 + N_2 \longleftrightarrow 2N + N_2$	4.7×10^{17}	-0.5	226000.0	2.72×10^{16}	-0.5	0.0
$NO + O_2 \longleftrightarrow N + O + O_2$	3.9×10^{20}	-1.5	151000.0	1.0×10^{20}	-1.5	0.0
$NO + N_2 \longleftrightarrow N + O + N_2$	3.9×10^{20}	-1.5	151000.0	1.0×10^{20}	-1.5	0.0
$NO + O \longleftrightarrow N + 2O$	7.8×10^{20}	-1.5	151000.0	2.0×10^{20}	-1.5	0.0
$NO + N \longleftrightarrow 2N + O$	7.8×10^{20}	-1.5	151000.0	2.0×10^{20}	-1.5	0.0
$NO + NO \longleftrightarrow N + O + NO$	7.8×10^{20}	-1.5	151000.0	2.0×10^{20}	-1.5	0.0
$N_2 + O \longleftrightarrow N + NO$	7.0×10^{13}	0.0	76000.0	1.56×10^{13}	0.0	0.0
$O + NO \longleftrightarrow N + O_2$	3.2×10^{9}	1.0	39400.0	1.3×10^{10}	1.0	7114.0

6 Conclusion

Shock/boundary-layer interactions (SBLI) is present in a wide range of applications in the aerospace industry. These complex phenomena are responsible for an increase of the aerodynamic drag and wall heat transfer rates, flow unsteadiness, and broadband noise emission. The literature about hypersonic SBLI is most of the time restricted to calorically perfect gases. This condition no longer holds in realistic flight conditions. High-temperature effects alter physical and transport properties of the fluid, due to vibrational excitation and gas dissociation, and chemical reactions must be considered in order to compute the flow field. In this work, a new solver was created and carefully validated based on a series of test-cases (2D laminar SBLI and turbulent boundary layer), in order to develop a numerical framework to perform direct numerical simulations of shock/boundary-layer interaction in chemical nonequilibrium. In other words, we presented a numerical recipe to simulate SBLI in chemical nonequilibrium. The numerical scheme and the characterization of non-reflecting boundary conditions were addressed. Classical NSCBC are not adapted to simulate this type of flow with realistic thermodynamics. The paper ends up with the simulation of the flow in the domain of interest, a shock-wave boundary layer interaction in chemical non-equilibrium for two configurations, a 2D incoming laminar boundary layer, and a 3D incoming turbulent boundary layer. Results showed that the flow properties differ considerably if chemical reactions are taken into account, even in the case of a laminar interaction. The analysis of statistical quantities showed that the turbulence activity is clearly modified after the reflecting shock foot and most of the reaction takes place after the interaction. Further studies are needed to understand the effects of chemical non-equilibrium in SBLI at higher Reynolds numbers and shock strengths.

Acknowledgments

This work was supported by the Air Force Office of Scientific Research (grant FA9550-16-1-0385) and performed using HPC resources at the University of Maryland (DeepThought2) and the Maryland Advanced Research Computing Center (MARCC).

1 Appendix: Numerical scheme coefficients

Table 4 Coefficients of the standard (S) and optimized (O) [32] schemes using 3-, 5-, 7-, 9- and 11-point stencils ($a_0 = 0$, $a_{-j} = -a_j$):

Coefficients	S2	S4	S6	S8	O4
a_1	1/2	2/3	3/4	4/5	0.872756993962
a_2		-1/12	-3/20	-1/5	-0.286511173973
a_3			1/60	4/105	0.090320001280
a_4				-1/280	-0.020779405824
a_4					0.002484594688

Table 5 Coefficients of the standard (S) and optimized (O) [32] filters using 3-, 5-, 7-, 9- and 11-point stencils ($d_{-j} = d_j$):

Coefficients	S2	S4	S6	S8	O4
d_0	0.5	0.375	0.3125	35/128	0.215044884112
d_1	-0.25	-0.25	-0.234375	-7/32	-0.187772883589
d_2		0.0625	0.09375	7/64	0.123755948787
d_3			-0.015625	-1/32	-0.059227575576
d_4				1/256	0.018721609157
d_4					-0.002999540835

2 Appendix: Thermo-chemistry validation

In order to validate the thermo-chemistry implementation, a mono-dimensional methane-air laminar flame was simulated at equivalence ratio $\phi = 0.83$ and compared with the AVBP solver solution [68]. A two-step reduced chemical mechanism for the methane oxidation presented in [69] was used in both runs:

$$\mathrm{CH_4} + 1.5\mathrm{O_2} \longrightarrow \mathrm{CO} + 2\mathrm{H_2O} \tag{42}$$

$$\mathrm{CO} + 0.5\mathrm{O_2} \longleftrightarrow \mathrm{CO_2} \tag{43}$$

The corresponding reaction rates are modeled using Arrhenius laws:

$$q_1 = A_1 T^{\beta_1} \exp\left(\frac{-E_{a1}}{RT}\right) \left(\frac{\rho Y_{\mathrm{CH_4}}}{W_{\mathrm{CH_4}}}\right)^{n^1_{\mathrm{CH_4}}} \left(\frac{\rho Y_{\mathrm{O_2}}}{W_{\mathrm{O_2}}}\right)^{n^1_{\mathrm{O_2}}} \tag{44}$$

$$q_2 = A_2 T^{\beta_2} \exp\left(\frac{-E_{a2}}{RT}\right) \left[\left(\frac{\rho Y_{\mathrm{CO}}}{W_{\mathrm{CO}}}\right)^{n^2_{\mathrm{CO}}} \left(\frac{\rho Y_{\mathrm{O_2}}}{W_{\mathrm{O_2}}}\right)^{n^2_{\mathrm{O_2}}} - \frac{1}{K_e} \left(\frac{\rho Y_{\mathrm{CO_2}}}{W_{\mathrm{CO_2}}}\right)^{n^2_{\mathrm{CO_2}}}\right] \tag{45}$$

where pre-exponential factors, activation energies and model exponents are summarized in Table 6. K_e is the equilibrium constant for the second reaction.

The reference viscosity is 1.8405×10^{-4} kg/(m.s), the reference temperature 300 K and the exponent for the power law 0.6759. The domain of length 1.6 cm was discretised in 400 equally distributed points.

Figure 20 compares the spatial evolution of mass fractions profiles, temperature, and heat capacity at constant pressure with the reference simulation. The agreement is excellent, validating the numerical implementation.

Table 6 Two-step reduced chemical mechanism for CH_4-Air. Coefficients for reaction rates [69]. Activation energies are in cal/mol and pre-exponential constants in cgs units.

Reaction	Coefficients	A_i	E_{ai}	β_i
1	$n^1_{CH_4} = 0.5$, $n^1_{O_2} = 0.65$	4.9×10^9	3.5×10^4	0
2	$n^2_{CO} = 1.0$, $n^2_{O_2} = 0.5$, $n^2_{CO_2} = 1.0$	2.0×10^8	1.2×10^4	0.7

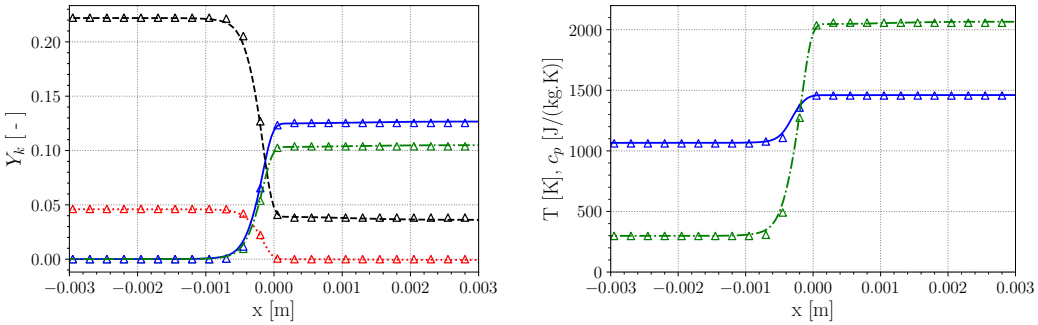

Fig. 20 Spatial evolution of mass fractions profiles (left), temperature, and heat capacity at constant pressure (right) for a 1D premixed methane/air flame at fresh gas temperature 300 K and pressure 1 atm. Left: Y_{CH_4} (dotted), Y_{O_2} (dashed), Y_{CO_2} (solid), Y_{H_2O} (dash-dotted). Right: c_p (solid) and temperature (dash-dotted). Symbols: AVBP solution.

References

1. G. S. Settles, S. M. Bogdonoff, and I. E. Vas. Incipient separation of a supersonic turbulent boundary layer at high reynolds numbers. *AIAA J.*, 14(1):50–56, 1976. URL `https://doi.org/10.2514/3.61331`.
2. F. O. Thomas, C. M. Putnam, and H. C. Chu. On the mechanism of unsteady shock oscillation in shock wave/turbulent boundary layer interactions. *Experiments in Fluids*, 18(1):69–81, 1994. URL `https://doi.org/10.1007/BF00209362`.
3. P. Dupont, C. Haddad, and J. F. Debieve. Space and time organization in a shock-induced separated boundary layer. *J. Fluid Mech.*, 559:255–277, 2006. URL `https://doi.org/10.1017/S0022112006000267`.
4. J. Délery and J.-P. Dussauge. Some physical aspects of shock wave/boundary layer interactions. *Shock waves*, 19(6): 453–468, 2009. URL `https://doi.org/10.1007/s00193-009-0220-z`.
5. S. Piponniau, J. P. Dussauge, J. F. Debieve, and P. Dupont. A simple model for low-frequency unsteadiness in shock-induced separation. *J. Fluid Mech.*, 629:87–108, 2009. URL `https://doi.org/10.1017/S0022112009006417`.
6. M. Bleilebens and H. Olivier. On the influence of elevated surface temperatures on hypersonic shock wave/boundary layer interaction at a heated ramp model. *Shock Waves*, 15(5):301–312, 2006. URL `https://doi.org/10.1007/s00193-006-0025-2`.
7. N. A. Adams. Direct simulation of the turbulent boundary layer along a compression ramp at M= 3 and Re_θ= 1685. *J. Fluid Mech.*, 420:47–83, 2000. URL `https://doi.org/10.1017/S0022112000001257`.
8. D. P. Rizzetta, M. R. Visbal, and D. V. Gaitonde. Large-eddy simulation of supersonic compression-ramp flow by high-order method. *AIAA J.*, 39(12):2283–2292, 2001. URL `https://doi.org/10.2514/2.1266`.
9. M. Wu and M. P. Martin. Analysis of shock motion in shockwave and turbulent boundary layer interaction using direct numerical simulation data. *J. Fluid Mech.*, 594:71–83, 2008. URL `https://doi.org/10.1017/S0022112007009044`.
10. S. Pirozzoli, A. Beer, M. Bernardini, and F. Grasso. Computational analysis of impinging shock-wave boundary layer interaction under conditions of incipient separation. *Shock Waves*, 19(6):487–497, 2009. URL `https://doi.org/10.1007/s00193-009-0215-9`.
11. E. Touber and N. D. Sandham. Large-eddy simulation of low-frequency unsteadiness in a turbulent shock-induced separation bubble. *Theoret. Comput. Fluid Dyn.*, 23(2):79–107, 2009. URL `https://doi.org/10.1007/s00162-009-0103-z`.
12. S. Pirozzoli and M. Bernardini. Direct numerical simulation database for impinging shock wave/turbulent boundary-layer interaction. *AIAA J.*, 49(6):1307–1312, 2011. URL `https://doi.org/10.2514/1.J050901`.
13. G. Aubard, X. Gloerfelt, and J.-C. Robinet. Large-eddy simulation of broadband unsteadiness in a shock/boundary-layer interaction. *AIAA J.*, 51(10):2395–2409, 2013. URL `https://doi.org/10.2514/1.J052249`.
14. G. M. Elfstrom. Turbulent hypersonic flow at a wedge-compression corner. *J. Fluid Mech.*, 53(1):113–127, 1972. URL `https://doi.org/10.1017/S0022112072000060`.
15. E. Schülein. Skin friction and heat flux measurements in shock/boundary layer interaction flows. *AIAA J.*, 44(8): 1732–1741, 2006. URL `https://doi.org/10.2514/1.15110`.
16. N. D. Sandham, E. Schülein, A. Wagner, S. Willems, and J. Steelant. Transitional shock-wave/boundary-layer interactions in hypersonic flow. *J. Fluid Mech.*, 752:349–382, 2014. URL `https://doi.org/10.1017/jfm.2014.333`.
17. L. Fu, M. Karp, S. T. Bose, P. Moin, and J. Urzay. Shock-induced heating and transition to turbulence in a hypersonic boundary layer. *Journal of Fluid Mechanics*, 909:A8, 2021. URL `https://doi.org/10.1017/jfm.2020.935`.
18. G. S. Settles and L. J. Dodson. Supersonic and hypersonic shock/boundary-layer interaction database. *AIAA J.*, 32 (7):1377–1383, 1994. URL `https://doi.org/10.2514/3.12205`.
19. J. D. Anderson Jr. *Hypersonic and high-temperature gas dynamics*. American Institute of Aeronautics and Astronautics, 2006.

20. P. A. Gnoffo. Planetary-entry gas dynamics. *Annual Review of Fluid Mechanics*, 31(1):459–494, 1999. URL https://doi.org/10.1146/annurev.fluid.31.1.459.
21. G. V. Candler. Rate effects in hypersonic flows. *Annual Review of Fluid Mechanics*, 51:379–402, 2019. URL https://doi.org/10.1146/annurev-fluid-010518-040258.
22. L. Duan and M. P. Martin. Direct numerical simulation of hypersonic turbulent boundary layers. part 4. effect of high enthalpy. *J. Fluid Mech.*, 684:25–59, 2011. URL https://doi.org/10.1017/jfm.2011.252.
23. M. Di Renzo and J. Urzay. Direct numerical simulation of a hypersonic transitional boundary layer at suborbital enthalpies. *Journal of Fluid Mechanics*, 912:A29, 2021. URL https://doi.org/10.1017/jfm.2020.1144.
24. J. L. Brown. Hypersonic shock wave impingement on turbulent boundary layers: Computational analysis and uncertainty. *J. Spacecr. Rockets*, 50(1):96–123, 2013. URL https://doi.org/10.2514/1.A32259.
25. S. Gordon and B. J. McBride. Computer program for calculation of complex chemical equilibrium compositions, rocket performance, incident and reflected shocks, and Chapman-Jouguet detonations. Technical report, NASA SP-273, 1976. URL https://ntrs.nasa.gov/citations/19780009781.
26. R. N. Gupta, J. M. Yos, R. A. Thompson, and K. P. Lee. A review of reaction rates and thermodynamic and transport properties for 11-species air model for chemical and thermal nonequilibrium calculation to 30,000 k. *NASA RP*, 1232, 1990. URL https://ntrs.nasa.gov/citations/19900017748.
27. C. R. Wilke. A viscosity equation for gas mixtures. *The journal of chemical physics*, 18(4):517–519, 1950. URL https://doi.org/10.1063/1.1747673.
28. K. K. Kuo. *Principles of combustion*. Wiley New York et al., 1986.
29. A. Jameson, W. Schmidt, and E. Turkel. Numerical solution of the euler equations by finite volume methods using runge kutta time stepping schemes. In *14th fluid and plasma dynamics conference*, page 1259, 1981. URL https://doi.org/10.2514/6.1981-1259.
30. M. R. Visbal and D. V. Gaitonde. High-order-accurate methods for complex unsteady subsonic flows. *AIAA J.*, 37 (10):1231–1239, 1999. URL https://doi.org/10.2514/2.591.
31. C. A. Kennedy and M. H. Carpenter. Several new numerical methods for compressible shear-layer simulations. *Applied Numerical Mathematics*, 14(4):397–433, 1994. URL https://doi.org/10.1016/0168-9274(94)00004-2.
32. C. Bogey and C. Bailly. A family of low dispersive and low dissipative explicit schemes for flow and noise computations. *J. Comput. Phys.*, 194(1):194–214, 2004. URL https://doi.org/10.1016/j.jcp.2003.09.003.
33. C. Bogey, N. De Cacqueray, and C. Bailly. A shock-capturing methodology based on adaptative spatial filtering for high-order non-linear computations. *J. Comput. Phys.*, 228(5):1447–1465, 2009. URL https://doi.org/10.1016/j.jcp.2008.10.042.
34. G. Aubard, P. S. Volpiani, X. Gloerfelt, and J.-C. Robinet. Comparison of subgrid-scale viscosity models and selective filtering strategy for large-eddy simulations. *Flow, turbulence and combustion*, 91(3):497–518, 2013. URL https://doi.org/10.1007/s10494-013-9485-5.
35. F. Ducros, F. Laporte, T. Souleres, V. Guinot, P. Moinat, and B. Caruelle. High-order fluxes for conservative skew-symmetric-like schemes in structured meshes: application to compressible flows. *J. Comput. Phys.*, 161(1):114–139, 2000. URL https://doi.org/10.1006/jcph.2000.6492.
36. G. W. Hedstrom. Nonreflecting boundary conditions for nonlinear hyperbolic systems. *J. Comput. Phys.*, 30(2):222–237, 1979. URL https://doi.org/10.1016/0021-9991(79)90100-1.
37. K. W. Thompson. Time dependent boundary conditions for hyperbolic systems. *J. Comput. Phys.*, 68(1):1–24, 1987. URL https://doi.org/10.1016/0021-9991(87)90041-6.
38. T. Poinsot and S. K. Lele. Boundary conditions for direct simulations of compressible viscous flows. *J. Comput. Phys.*, 101(1):104–129, 1992. URL https://doi.org/10.1016/0021-9991(92)90046-2.
39. M. Baum, T. J. Poinsot, D. C. Haworth, and N. Darabiha. Direct numerical simulation of h 2/o 2/n 2 flames with complex chemistry in two-dimensional turbulent flows. *J. Fluid Mech.*, 281:1–32, 1994. URL https://doi.org/10.1017/S0022112094003010.
40. N. Okong'o and J. Bellan. Consistent boundary conditions for multicomponent real gas mixtures based on characteristic waves. *J. Comput. Phys.*, 176(2):330–344, 2002. URL https://doi.org/10.1006/jcph.2002.6990.
41. W. Pakdee and S. Mahalingam. An accurate method to implement boundary conditions for reacting flows based on characteristic wave analysis. *Combustion theory and modelling*, 7(4):705–729, 2003. URL https://doi.org/10.1088/1364-7830/7/4/006.
42. T. Poinsot and D. Veynante. *Theoretical and numerical combustion*. www.cerfacs.fr/elearning, 3rd edition, 2011.
43. X. Gloerfelt and P. Lafon. Direct computation of the noise induced by a turbulent flow through a diaphragm in a duct at low mach number. *Computers & fluids*, 37(4):388–401, 2008. URL https://doi.org/10.1016/j.compfluid.2007.02.004.
44. G. Degrez, C. H. Boccadoro, and J. F. Wendt. The interaction of an oblique shock wave with a laminar boundary layer revisited. an experimental and numerical study. *J. Fluid Mech.*, 177:247–263, 1987. URL https://doi.org/10.1017/S0022112087000946.
45. A. Gross and H. F. Fasel. Numerical investigation of shock boundary-layer interactions. In *54th AIAA Aerospace Sciences Meeting*, page 0347, 2016. URL https://doi.org/10.2514/6.2016-0347.
46. I. B. H. Saïdi, C. Tenaud, and G. Fournier. Solving three dimensional turbulent compressible flows using a high order one step monotony preserving scheme. In *10th International Conference on Computational Fluid Dynamics (ICCFD10)*, pages 10–114, 2018. URL https://hal.archives-ouvertes.fr/hal-02187216.
47. J. Larsson and S. K. Lele. Direct numerical simulation of canonical shock/turbulence interaction. *Physics of Fluids*, 21(12):126101, 2009. URL https://doi.org/10.1063/1.3275856.
48. E. Johnsen, J. Larsson, A. V. Bhagatwala, W. H. Cabot, P. Moin, B. J. Olson, P. S. Rawat, S. K. Shankar, B. Sjögreen, H. C. Yee, et al. Assessment of high-resolution methods for numerical simulations of compressible turbulence with shock waves. *J. Comput. Phys.*, 229(4):1213–1237, 2010. URL https://doi.org/10.1016/j.jcp.2009.10.028.
49. L. Selle, F. Nicoud, and T. Poinsot. Actual impedance of nonreflecting boundary conditions: Implications for computation of resonators. *AIAA journal*, 42(5):958–964, 2004. URL https://doi.org/10.2514/1.1883.
50. G. Lodato, P. Domingo, and L. Vervisch. Three-dimensional boundary conditions for direct and large-eddy simulation of compressible viscous flows. *Journal of computational physics*, 227(10):5105–5143, 2008. URL https://doi.org/10.1016/j.jcp.2008.01.038.

51. M. Klein, A. Sadiki, and J. Janicka. A digital filter based generation of inflow data for spatially developing direct numerical or large eddy simulations. *J. Comput. Phys.*, 186(2):652–665, 2003. URL https://doi.org/10.1016/S0021-9991(03)00090-1.
52. Z. T. Xie and I. P. Castro. Efficient generation of inflow conditions for large eddy simulation of street-scale flows. *Flow, turbulence and combustion*, 81(3):449–470, 2008. URL https://doi.org/10.1007/s10494-008-9151-5.
53. M. C. Adler, D. R. Gonzalez, C. M. Stack, and D. V. Gaitonde. Synthetic generation of equilibrium boundary layer turbulence from modeled statistics. *Computers & Fluids*, 165:127–143, 2018. URL https://doi.org/10.1016/j.compfluid.2018.01.003.
54. T. S. Lund, X. Wu, and K. D. Squires. Generation of turbulent inflow data for spatially-developing boundary layer simulations. *J. Comput. Phys.*, 140(2):233–258, 1998. URL https://doi.org/10.1006/jcph.1998.5882.
55. P. Schlatter and R. Örlü. Assessment of direct numerical simulation data of turbulent boundary layers. *J. Fluid Mech.*, 659:116, 2010. URL https://doi.org/10.1017/S0022112010003113.
56. S. Pirozzoli and M. Bernardini. Turbulence in supersonic boundary layers at moderate reynolds number. *J. Fluid Mech.*, 688:120–168, 2011. URL https://doi.org/10.1017/jfm.2011.368.
57. P. S. Volpiani, M. Bernardini, and J. Larsson. Effects of a nonadiabatic wall on supersonic shock/boundary-layer interactions. *Phys. Rev. Fluids*, 3:083401, Aug 2018. URL https://link.aps.org/doi/10.1103/PhysRevFluids.3.083401.
58. E. J. Hopkins and M. Inouye. An evaluation of theories for predicting turbulent skin friction andheat transfer on flat plates at supersonic and hypersonic mach numbers. *AIAA J.*, 9(6):993–1003, 1971. URL https://doi.org/10.2514/3.6323.
59. H. Schlichting and K. Gersten. *Boundary-layer theory*. Springer, 2016.
60. L. Duan and M. P. Martin. Effect of finite-rate chemical reactions on turbulence in hypersonic turbulence boundary layers. In *47th AIAA Aerospace Sciences Meeting Including The New Horizons Forum and Aerospace Exposition*, page 588, 2009. URL https://doi.org/10.2514/6.2009-588.
61. P. Kim. *Non-equilibrium effects on hypersonic turbulent boundary layers*. PhD thesis, UCLA, 2016. URL https://escholarship.org/uc/item/6mb1p42d.
62. P. S. Volpiani, M. Bernardini, and J. Larsson. Effects of a nonadiabatic wall on hypersonic shock/boundary-layer interactions. *Phys. Rev. Fluids*, 5:014602, Jan 2020. URL https://link.aps.org/doi/10.1103/PhysRevFluids.5.014602.
63. C. J. Roy and F. G. Blottner. Review and assessment of turbulence models for hypersonic flows. *Progress in Aerospace Sciences*, 42(7-8):469–530, 2006. URL https://doi.org/10.1016/j.paerosci.2006.12.002.
64. M. Hayashi, A. Sakurai, and S. Aso. Measurement of heat-transfer coefficients in shock wave-turbulent boundary layer interaction regions with a multi-layered thin film heat transfer gauge. *NASA STI/Recon Technical Report N*, 86, 1986. URL https://ntrs.nasa.gov/citations/19860012319.
65. L. J. Souverein, P. G. Bakker, and P. Dupont. A scaling analysis for turbulent shock-wave/boundary-layer interactions. *J. Fluid Mech.*, 714:505–535, 2013. URL https://doi.org/10.1017/jfm.2012.495.
66. V. Jaunet, J. F. Debiève, and P. Dupont. Length scales and time scales of a heated shock-wave/boundary-layer interaction. *AIAA J.*, 52(11):2524–2532, 2014. URL https://doi.org/10.2514/1.J052869.
67. M. G. Dunn and S. Kang. Theoretical and experimental studies of reentry plasmas. Technical report, NASA CR-2232, 1973. URL https://ntrs.nasa.gov/citations/19730013358.
68. V. Moureau, G. Lartigue, Y. Sommerer, C. Angelberger, O. Colin, and T. Poinsot. Numerical methods for unsteady compressible multi-component reacting flows on fixed and moving grids. *J. Comput. Phys.*, 202(2):710–736, 2005. URL https://doi.org/10.1016/j.jcp.2004.08.003.
69. B. Franzelli, E. Riber, L. Y. M. Gicquel, and T. Poinsot. Large eddy simulation of combustion instabilities in a lean partially premixed swirled flame. *Combustion and flame*, 159(2):621–637, 2012. URL https://doi.org/10.1016/j.combustflame.2011.08.004.